

## High and low energy nucleon productions in intermediate heavy ion collisions, using AMD with Fermi boost and 3-body collision terms

R. WADA<sup>(2)</sup>(\*), Q. HU<sup>(1)</sup>, G. TIAN<sup>(1)</sup>, W. LIN<sup>(3)</sup>, Z. CHEN<sup>(1)</sup>, R. HAN<sup>(1)</sup>, X. LIU<sup>(3)</sup>, M. HUANG<sup>(4)</sup> and H. ZHENG<sup>(5)</sup>

<sup>(1)</sup> *Institute of Modern Physics, Chinese Academy of Sciences - Lanzhou 730000, China*

<sup>(2)</sup> *Cyclotron Institute, Texas A&M University - College Station, TX 77843, USA*

<sup>(3)</sup> *Key Laboratory of Radiation Physics and Technology of the Ministry of Education, Institute of Nuclear Science and Technology, Sichuan University - Chengdu 610064, China*

<sup>(4)</sup> *College of Physics and Electronics information, Inner Mongolia University for Nationalities Tongliao, 028000, China*

<sup>(5)</sup> *School of Physics and Information Technology, Shaanxi Normal University - Xi'an 710119, China*

received 12 May 2022

**Summary.** — The effect of a Fermi boost and 3 nucleon (3N) collision terms are studied in the framework of the anti-symmetrized molecular dynamics (AMD) of Ono *et al.* in two extreme cases of intermediate heavy ion collisions, one for the production of high energy nucleons and the other for the hydrogen target with heavier projectiles. The Fermi boost is added in the binary collision process as a fluctuation in the momentum space for colliding two nucleons. The 3N collision term is incorporated using a diagram of three consecutive binary collisions. The model is applied to the available experimental data and the high energy nucleon yields are well reproduced at the incident energy range of 44 A MeV to 400 A MeV. The Fermi boost is effective for the high energy proton production at the incident energy below 50 A MeV. While above 50 A MeV, the 3N collision term becomes dominant. The model is also applied for the proton emission from  $^{12}\text{C} + ^1\text{H}$  at 95 A MeV. The experimental data are also well reproduced by these models.

### 1. – Introduction

In this talk, I will present our recent results for nucleon productions in two extreme cases, using AMD. AMD codes have been written in several versions [1-6]. All results shown below are based on refs. [2,3] version. In this version, a diffusion process is incorporated on the original AMD of ref. [1] and called AMD/D. AMD is a transport model

(\*) E-mail: wada@comp.tamu.edu

with  $N$  Gaussian wave packets, where  $N$  is the number of nucleons in the system. In order to respect the Pauli principle in the mean field and collision process at the whole reaction time, the wave packets are anti-symmetrized. AMD uses a frozen concept for the initial nuclei at their ground state, which means that the centroid of the momentum wave packets of these initial nuclei are set to nearly zero and the Fermi motion is only taken into account as an average energy of the wave packet in the energy calculation. The equation of motion is solved with the Vlasov equation with the centroid of these wave packets. Therefore, their trajectories are essentially classical. This causes a serious problem when it is applied to the  $^{40}\text{Ca} + ^{40}\text{Ca}$  collisions at  $35 A \text{ MeV}$ . The projectile  $^{40}\text{Ca}$  often punches through the target and appears on the opposite side even for head-on collisions, though they are generally excited when passing through the target. This strong transparency is not observed in the experimental data. In order to improve the wave packet behavior, momentum fluctuations are explicitly taken into account during the time evolution of the wave packets in the mean field. This fluctuation is incorporated stochastically along the Vlasov equation in every time step. This process is called “diffusion” process, since it corresponds to a quantum branching of the wave packet during the time evolution and enhances the multi-fragmentation process. This version is called AMD/D. This treatment significantly improves the reproduction of the experimental data in their charge distribution [2]. AMD/D generally reproduces the experimental results in the intermediate heavy ion collisions reasonably well [2, 5, 7-9]. However, when these models are applied in extreme cases, they often reveal missing underlined physics, if any. We applied AMD/D in two extreme cases: one is the high energy nucleon production and the other is the reaction with hydrogen target.

## 2. – High energy proton/neutron production

Beautiful experimental data sets for the high energy proton production are available. One was performed at GANIL in late 1990’s using the  $4\pi$  MEDEA array for  $^{40}\text{Ar} + ^{51}\text{V}$  at  $44 A \text{ MeV}$  [10]. The array consists of 120 phoswich  $\text{BaF}_2$  forward wall and 180  $\text{BaF}_2$  ball, covered  $10^\circ$  to  $170^\circ$ . It is made primarily for gamma detection, but it provides good p, d, t identifications. The energy of the protons in each  $\text{BaF}_2$  was calibrated using cosmic muons at their maximum energy loss of 134 MeV in 20 cm  $\text{BaF}_2$  crystal. AMD/D is applied for the proton energy spectra in the center-of-mass system, and the results are shown in fig. 1(a) with red histograms. AMD/D totally fails to reproduce the high energy proton yields at all angles. One should note that the energy range of the discrepancies between the experimental data and the AMD simulation is 50 to 200 MeV, which is much larger than the mean kinetic energy of the projectile and target protons. There are some hints for the failure. When the diffusion process is turned off, the results become worse (blue histogram). This indicates that the diffusion process improves the reproduction of the high energy proton yields, but not far enough. As mentioned in the introduction, the diffusion process originates from the Fermi motion and is taken into account in the wave packet propagation in the mean field, but not in the binary collision process. Therefore, we incorporate the Fermi motion when two nucleons collide with each other. We add the momentum fluctuation, which is randomly given according to the Gaussian wave packet, to the momentum of two colliding nucleons individually.

This treatment works very well as shown by the blue histogram in fig. 1(b). This new version is called AMD-FM and this process is called “Fermi boost”. More detail descriptions are given in ref. [11]. AMD-FM is further applied to the available data at higher incident energies,  $^{40}\text{Ar} + ^{40}\text{Ca}$  at  $92 A$  and  $137 A \text{ MeV}$ , which were taken at

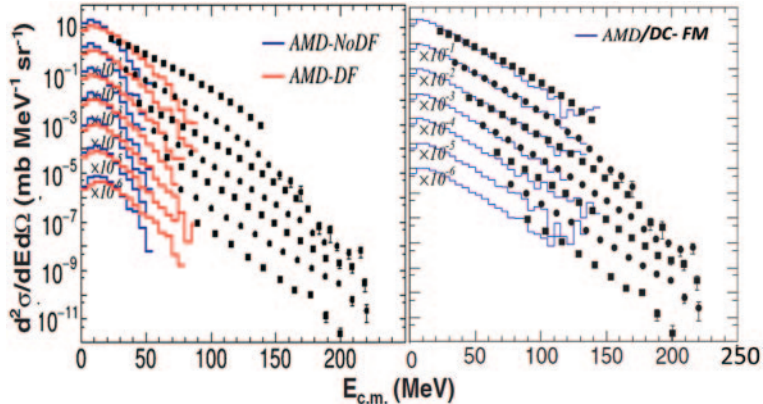


Fig. 1. – (Color online). The Center of Mass frame proton energy spectra for  $^{40}\text{Ar} + ^{51}\text{V}$  at  $44 A$  MeV (closed symbols) with AMD results. (a) Red histograms represent the results from AMD/D and the blue histograms are those without the diffusion process. The experimental data correspond to the energy spectra at  $\theta = 72^\circ, 90^\circ, 104^\circ, 116^\circ, 128^\circ, 142^\circ$  and  $160^\circ$  from the top to the bottom. The experimental data are taken from [12]. (b) Comparisons with the AMD-FM results. All results are plotted in an absolute scale, but they are multiplied by a factor of  $10^{-n}$  ( $n = 0$  to  $6$ ) from the top to the bottom.

BEVALAC in late 1970's. The AMD-FM results with the diffusion process (AMD/D-FM) are plotted by the dashed curves with the experimental data on the two right panels in fig. 2. AMD-FM again fails to reproduce the experimental data severely for the high energy proton production at these high incident energies. A similar observation was made by Germain *et al.* [13] in 1997. They compared the experimentally observed high energy proton spectra from  $^{36}\text{Ar} + ^{181}\text{Ta}$  at  $94 A$  MeV to BNV simulations with an extra caution of the Fermi motion. The binary collisions alone did not reproduce the experimental yields, but when they added a 3N collision contribution, which was evaluated from the BNV density distribution, the experimental yields were reproduced reasonably well. This evaluation was followed to the Mrowczynski's formulation given in [14]. In his formulation, the 3N collision is described as three-consecutive binary collisions and the 3N collision cross section,  $C_3$ , is given as

$$(1) \quad C_3 = \frac{16}{3\sqrt{\pi}} \sigma^{3/2} \rho^3 T^{1/2},$$

where  $\sigma$  is the 2N collision cross section,  $\rho$  is the nuclear matter density and  $T$  is the temperature, which are originated from the assumption of their uniform energy and matter distributions. In the actual AMD application,  $\rho$  and  $T$  are not used, since the AMD collision rate is automatically taken into account by these factors in the collision process. A constant value of  $\sigma = 33$  mb is used for the following calculations. When three nucleons are within the collision distance in each other at a given time step, the 3N collision is examined. Randomly selected three of binary pairs are sequentially examined for collisions and only the final states of the three nucleons are examined for the Pauli-blocking. When the collision is Pauli-allowed, the energy conservation is restored, by adjusting the position and momentum of the other nucleons surrounded by these three nucleons along the Vlasov equation. One should note that this process is quite different

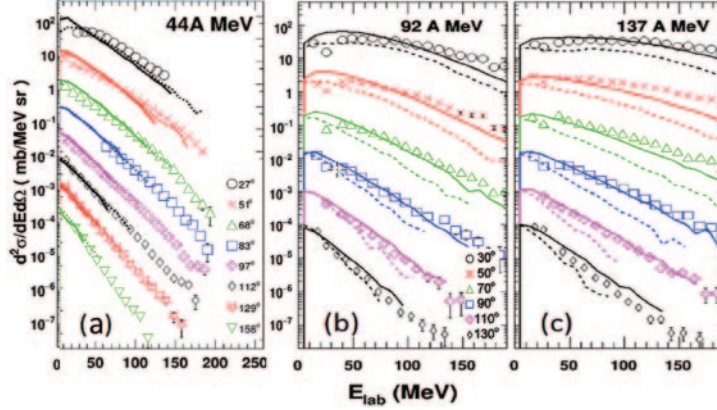


Fig. 2. – (Color online). Experimental results of proton energy spectra are compared with the simulated AMD results for the  $^{40}\text{Ar} + ^{51}\text{V}$  reactions at (a) 44 *A* MeV, (b)  $^{40}\text{Ar} + ^{40}\text{Ca}$  reactions at 92 *A* MeV and (c) 137 *A* MeV. Data (a) are from ref. [12] and (b), (c) are taken from ref. [15]. Solid curves are for the results of AMD-3NC and dashed curves are from those of AMD-FM. Data and results are plotted in an absolute scale. All results are multiplied by a factor of  $10^{-n}$  ( $n = 0$  to 8 in (a) and 5 in (b) and (c)) from the top to the bottom for clarity.

from the binary collision process in the AMD calculation. When the ternary collision process is turned off, three pairs of binary collisions are examined in the same situation. However, when the first pair is Pauli-allowed, then the other two pairs of the collision are canceled, since at most one collision is allowed for each nucleon at a given time step. If the first one is Pauli-blocked, then the second pair is examined and so on. The probability of a binary collision increases three times, but they are still a binary collision. On the other hand, in a ternary collision three nucleons suffer two collisions in the time step and at their intermediate stage, the collisions are assumed in a virtual state, which means no Pauli condition is applied. Therefore, one of three nucleons can have a chance to get most of the other nucleon's kinetic energy and emerges as a high energy nucleon in their rest frame. This new version is called AMD-FM(3N) or simply AMD-3NC. A detailed description is also given in ref. [16].

AMD-3NC is applied to the BEVALAC data as shown in fig. 2 with solid curves. It reproduces the experimental data reasonably well at all experimentally observed angles at higher energies, especially on the two right figures. On the left the results for the MEDEA data are also shown in the laboratory frame. At 44 *A* MeV no noticeable difference is observed in the results between AMD-FM and AMD-3NC. On the left in fig. 3, the number of 2N (red) and 3N (black) collisions is plotted as a function of the reaction time. Open symbols represent the attempted collisions and the closed are for the Pauli-allowed collisions. Both of the collisions show a peak at the early stage of the reaction, but 2N collisions occur up to  $t = 300$  fm/*c* continuously in both attempted and Pauli-allowed ones. On the other hand, 3N collisions occur only at the time span of 10–40 fm/*c*, a narrower time span for the higher incident energy. This indicates that the enhanced proton cross sections observed on the high energy side in the two right panels of fig. 2 are dominated by those emitted by the 3N collisions at a high density hot nuclear matter. Therefore, they may provide a unique probe to study the hot-high density nuclear matter. On the right of fig. 3, the number of collisions is plotted as a function of the

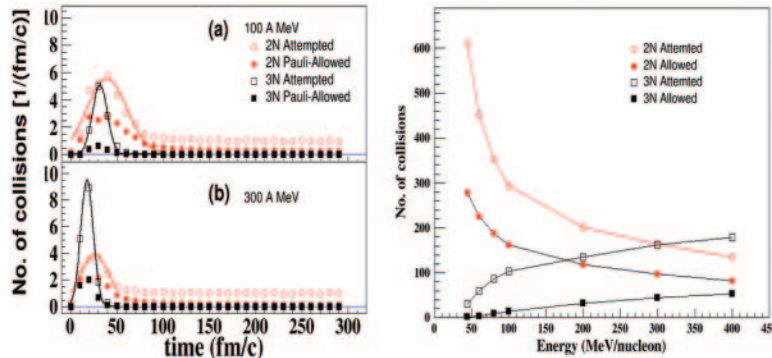


Fig. 3. – (Color online). Left: number of 2N (circles) and 3N (squares) collisions are plotted as a function of the reaction time. Curves are from Gaussian fits for the attempted collisions near the peaks. (a)  $^{40}\text{Ar} + ^{51}\text{V}$  at 100 A MeV. The density in the overlap region becomes maximum at  $\sim 30$  fm/c at this energy. (b)  $^{40}\text{Ar} + ^{51}\text{V}$  at 300 A MeV. The density becomes maximum at  $\sim 20$  fm/c at this energy. The sigma values of the Gaussian are 21.7 (15.9) for 2N and 8.0 (6.8) for 3N attempted collisions at 100 A (300 A) MeV, respectively. Right: the number of 2N (circles) and 3N (squares) collisions, integrated over the time between  $t = 0$  to  $t = 300$  fm/c, are plotted as a function of incident energy.

incident energy. The number of 2N collisions decreases rapidly up to 100 A MeV and slowly decreases above that energy. This is related to the decrease of the free nucleon-nucleon cross sections. About 50% of the attempted 2N collisions are Pauli-blocked. The number of 3N collisions increases slowly and reaches about one third of that of the 2N collisions at 400 A MeV. About two third of 3N collisions are Pauli-blocked, even at 400 A MeV. The number of the Pauli-allowed 2N and 3N collisions are comparable at 400 A MeV.

We further compare the AMD-3NC results to the high energy neutron production data. The available data were taken by two independent groups at the HIMAC facility in the National Institute of Radiological Sciences (NRIS), Japan. Neutron spectra were measured, using the TOF technique. In ref. [17],  $^{12}\text{C}$ ,  $^{20}\text{Ne}$  and  $^{40}\text{Ar}$  beams were bombarded on C, Cu and Pb targets at 290 A MeV to 560 A MeV range. In ref. [18],  $^{12}\text{C}$ ,  $^{16}\text{O}$  were bombarded on C target at 290 A MeV. Here we only show the AMD results for the  $^{12}\text{C} + ^{12}\text{C}$  reactions. At 290 A MeV, some of the angles measured were the same in the two experiments, but in fig. 4 both results are combined and plotted with different symbols. AMD-FM and AMD-3NC results are shown by histograms. The difference between two AMD results becomes smaller than the one observed in fig. 2, since the maximum density achieved at the early stage of the reaction becomes smaller for the  $^{12}\text{C} + ^{12}\text{C}$  cases. One can clearly see good reproductions of high energy neutron yields with AMD-3NC for both experimental data sets. In fig. 5 the comparisons are made at 400 A MeV. Only AMD-3NC results are compared, but the experimental data are reproduced at the high energy side reasonably well.

### 3. – Protons from $^{12}\text{C} + ^1\text{H}$ reaction

We move on to the second extreme case of the Hydrogen target. The available experimental data were taken at GANIL, using five Si-Si-CsI telescopes for dosimetry [19]. Light charged particles were measured at 20 angles from  $4^\circ$  to  $43^\circ$ . A variety of targets

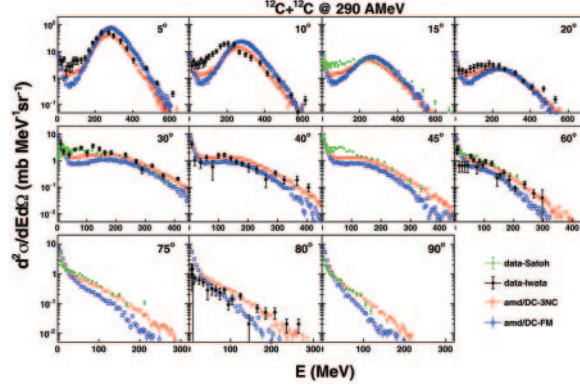


Fig. 4. – (Color online). Neutron energy distributions for  $^{12}\text{C} + ^{12}\text{C}$  at 290 A MeV. The experimental data from ref. [17] and [18] are combined together in these plots, where the former data are represented by black symbols and the latter by green symbols. The results for AMD-FM and AMD-3NC are plotted by blue and red symbols, respectively.

were bombarded with  $^{12}\text{C}$  at 95 A MeV, but here we only compare the proton energy spectra from the  $^{12}\text{C} + ^1\text{H}$  reaction with AMD simulations. The  $^{12}\text{C} + ^1\text{H}$  reaction data were obtained by subtracting the  $^{12}\text{C} + ^{12}\text{C}$  data from the  $^{12}\text{C} + \text{CH}_2$  data.

First we compare the AMD results. In fig. 6, 2D ( $v_z$  vs.  $v_t$ ) velocity plots of protons are shown for the AMD simulations with different stochastic processes.  $v_z$  is the velocity of the beam direction.  $v_t$  is the transverse velocity and assigned positive for the azimuthal angle  $0^\circ \leq \phi < 180^\circ$  and negative otherwise. On the top row, the primary proton distribution with the original AMD is shown on the left and that of the final product after the afterburner, GEMINI, is on the right. In both cases, a clear ring is observed. This ring is generated from the quasi-elastic scattering between the target proton and one of nucleons in the projectile. In AMD, the target proton does not see the  $^{12}\text{C}$  projectile as a whole, since AMD is based on a nucleon-nucleon interaction. The quasi-elastically scattered protons are distributed in a ring centered at the half beam velocity. The final

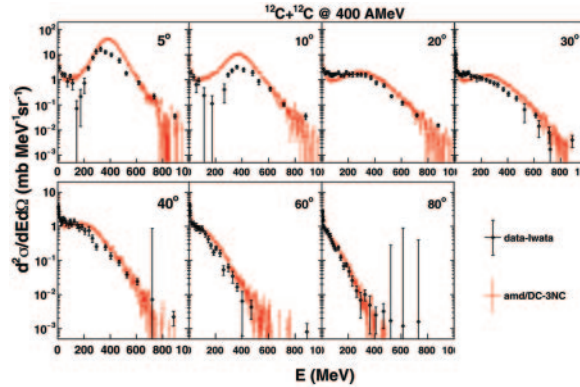


Fig. 5. – (Color online). Similar plots as fig. 4, but at 400 A MeV. Only the AMD-3NC results are compared with the experimental data.

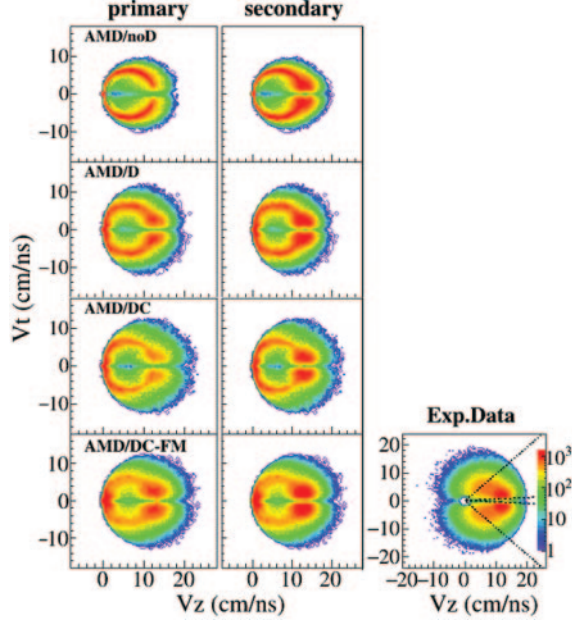


Fig. 6. – (Color online). 2D velocity distributions for simulated protons are plotted for AMD/noD, AMD/D, AMD/D-COALS and AMD-FM from the top to the bottom, respectively. The velocity spectra for the primary protons are plotted on the left column and those for the secondary on the right column. On the bottom far right, the reconstructed experimental distribution is shown, which is generated using the moving source parameters. Similar number of events are used for each plot.

proton distribution on the right indicates the additional protons near the beam velocity, which originate from the excited projectile-like fragments (PLF), mostly  $^{12}\text{C}$ . They move with the beam velocity and emit protons in the secondary cooling process. No protons from the excited PLFs are observed before  $t = 300$  fm/c, the end of the AMD dynamical calculation time. In the second row similar distributions, but with the diffusion process ON, are shown. One can see two clear effects of the diffusion process in the primary stage on the left, one is the broadening of the ring width and the other is the PLF protons. These are very reasonable results one can expect from the diffusion process incorporated. As mentioned earlier, the diffusion process is introduced to add momentum fluctuations during the time evolution of the wave packets, which also recovers the quantum nature in the particle emissions. The former contributes to the broadening of the ring and the latter accelerates the particle emission from the hot PLFs. However, the proton emissions from the excited PLFs do not exhaust the available excitation energy before  $t = 300$  fm/c. About 50% of the excitation energy remains and is exhausted in GEMINI by the secondary emissions. On the third row, the results with a coalescence process are shown. The original AMD provides a coalescence subroutine, which is turned off for the default setting. This subroutine makes nucleon coalesce up to  $A = 4$  (alpha) particles when they are within a coalescence radius of 2.5 fm with proper isospin combinations. Details are described in ref. [20]. When a quasi-elastically scattered proton emitted near the projectile, it has a chance to find nucleons nearby and is coalesced with them to form a light cluster. Once clusterization occurs, the proton disappears from the plot.

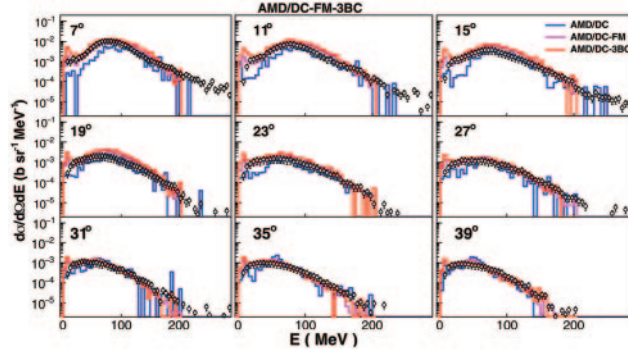


Fig. 7. – (Color online). Proton energy spectra for the experiment, AMD/DC, AMD-FM, AMD-3NC are presented at selected nine angles. Symbols are from the experimental data and histograms are from the AMD simulations.

This is why the ring width becomes slim near the projectile. When the Fermi boost is turned on, the results are shown in two bottom figures. They become similar to those of the AMD/D, but quantitative comparisons are difficult to make in the 2D plot. The experimental velocity distribution is made from the events generated using a moving source parameterization and plotted on the bottom right. One should note that the experimental data exist only in the area between the two dashed lines ( $3^\circ \leq \theta \leq 43^\circ$ ). Quantitative comparisons between the reconstructed experimental distribution and those of AMDs are presented in fig. 7.

In fig. 7 the above AMD/DC, AMD-FM and AMD-3NC results are compared with the experimental data at selected nine angles. The AMD results with the diffusion and coalescence processes (AMD/DC) are plotted with blue histograms. Significant underpredictions are clearly seen at the low energy side at almost all angles. The figure also shows a small peak around 50 MeV at the last two angles, corresponding to the quasi-elastic ring observed in fig. 6. AMD-FM improves the low energy proton production, but shows a peak near zero energy. This originates from momentum fluctuation of the target protons when they are passing through the projectile. Experimentally these low energy protons are mostly cut off by the detector threshold. The AMD results are filtered by the experimental limitations, but the low energy threshold is taken from the detector thickness alone and the particle identification threshold is unknown. AMD-3NC results are almost identical to those of AMD-FM, since no compression is occurred in the Hydrogen target even at 95 A MeV.

#### 4. – Summary

AMD models are applied for two extreme cases, one for the high energy nucleon emission and the other for the Hydrogen target reaction. High energy proton yields in the intermediate energy heavy ion collisions below 50 A MeV are well reproduced with AMD-FM, where a new Fermi boost is incorporated in the binary collision process in the original AMD with the diffusion process. Above 50 A MeV, the added 3N collision process becomes important and AMD-3NC reproduces the high energy proton and neutron yields at the incident energy range of 100 A–400 A MeV. The 3N collisions are enhanced in the high density nuclear matter and therefore they only occur at the early stage of the

reactions in the intermediate heavy ion collisions. This indicates that the high energy nucleons may provide a unique probe to study the high-density hot nuclear matter.

AMD-FM and AMD-3NC are also applied to the  $^{12}\text{C} + ^1\text{H}$  reaction at 95 A MeV. 2D plot reveals the distinct role of the different stochastic processes incorporated in the AMD. The experimental data are well reproduced with AMD-FM. No noticeable difference is observed between AMD-FM and AMD-3NC, indicating that no high density area is created at the early stage of the reaction in the  $^{12}\text{C} + ^1\text{H}$  reaction at 95 A MeV.

\* \* \*

We thank A. Ono for providing his AMD source code. We also thank A. Bonasera for useful discussions. This work is also supported by the US Department of Energy under Grant No. DE-FG02-93ER40773.

## REFERENCES

- [1] ONO A. and HORIUCHI H., *Prog. Theor. Phys.*, **87** (1992) 1185.
- [2] ONO A., *Phys. Rev. C*, **53** (1996) 2958.
- [3] ONO A., *Phys. Rev. C*, **59** (1999) 853.
- [4] ONO A. *et al.*, *Phys. Rev. C*, **66** (2002) 014603.
- [5] TIAN G. *et al.*, *Phys. Rev. C*, **95** (2017) 044613.
- [6] ILENO N. *et al.*, *Phys. Rev. C*, **93** (2016) 044612.
- [7] WADA R. *et al.*, *Phys. Rev. C*, **69** (2004) 044610.
- [8] HAN R. *et al.*, *Phys. Rev. C*, **102** (2020) 064617.
- [9] ONO A. and HORIUCHI H., *Prog. Part. Nucl. Phys.*, **53** (2004) 501.
- [10] MIGNECO E. *et al.*, *Nucl. Phys. A*, **314** (1992) 31.
- [11] LIN W. *et al.*, *Phys. Rev. C*, **92** (2015) 014623.
- [12] CONIGLIONE R. *et al.*, *Phys. Lett. B*, **47** (2000) 339.
- [13] GERMAIN M. *et al.*, *Nucl. Phys. A*, **620** (1997) 81.
- [14] MRÓWCZYŃSKI ST., *Phys. Rev. C*, **32** (1985) 1784.
- [15] KRUSE H. *et al.*, *Phys. Rev. C*, **31** (1985) 1770.
- [16] WADA R., *Phys. Rev. C*, **96** (2017) 031601.
- [17] IWATA Y. *et al.*, *Phys. Rev. C*, **64** (2001) 054609.
- [18] SATOH D. *et al.*, *Nucl. Instrum. Methods A*, **644** (2011) 59.
- [19] DUDOUE J. *et al.*, *Phys. Rev. C*, **88** (2013) 024606.
- [20] ONO A., *Prog. Theor. Phys. Suppl.*, **140** (2000) 134.